

The effect of nanochannel length on *in situ* loading times of diffusion-propelled nanoparticles in liquid cell electron microscopy

Peter Kunnas^{a,b}, Niels de Jonge^{c,d,e}, Joseph P. Patterson^{f,*}

^a University of Vienna, Faculty of Physics, VCQ, Vienna A-1090, Austria

^b University of Vienna, Max Perutz Laboratories, Department of Structural and Computational Biology, Vienna A-1030, Austria

^c Leibniz Institute for New Materials, Saarbrücken, Germany

^d Department of Physics, Saarland University, Saarbrücken, Germany

^e Bruker AXS, Karlsruhe, Germany

^f Department of Chemistry, University of California Irvine, Irvine, CA 92697-2025, United States

ARTICLE INFO

Keywords:

Nanofluidics

Liquid cell electron microscopy

Scanning transmission electron microscopy

Nanoparticle

Diffusion

Self-assembled monolayer

ABSTRACT

Liquid cell transmission electron microscopy is a powerful tool for visualizing nanoparticle (NP) assemblies in liquid environments with nanometer resolution. However, it remains a challenge to control the NP concentration in the high aspect ratio liquid enclosure where the diffusion of dispersed NPs is affected by the exposed surface of the liquid cell walls. Here, we introduce a semi-empirical model based on the 1D diffusion equation, to predict the NP loading time as they pass through the nanochannel into the imaging volume of the liquid cell. We show that loading of NPs into the imaging volume of the liquid cell may take several days if NPs are prone to attach to the surface of the mm-long nanochannel when using an industry-standard flat microchip. As a means to facilitate mass transport via diffusion, we tested a liquid cell incorporating a microchannel geometry resulting in a NP loading time in the order minutes that allowed us to observe the formation of a randomly oriented self-assembled monolayer *in situ* using scanning transmission electron microscopy.

1. Introduction

One of the grand challenges in soft matter science is to understand how dispersed nanoparticles (NP) self-assemble into larger superstructures that possess significant potential in application areas such as catalysis and photonics [1]. Direct visualization has been proposed as a tool to map the experimental phase behavior of NP dispersions for guiding the development of molecular simulations with improved predictive capability toward extended NP systems [2]. Liquid cell electron microscopy (LCEM) can visualize the structure and dynamics of colloidal NP assemblies from nanometer resolution [3] to the mesoscopic scale [4]. However, in order to fully utilize the impressive resolving power of LCEM [5], the sample must be thin, causing a degree of confinement different from that of a bulk sample. To this day, it remains a challenge to supply dispersed NPs into the confined liquid enclosure *in situ* and observe bulk-like phase behavior and subsequent self-assembly into superstructures such as colloidal crystals [6] or self-assembled monolayers (SAM) [7].

The common liquid enclosure employed in LCEM is a high-aspect

ratio nanochannel constructed out of two opposing flat microchips, separated by a spacer layer of thickness typically in the range of 0.1 to a few μm . The microchip fabrication process utilizes chemical vapor deposition (CVD) and anisotropic etching steps [8] to create a rectangular, 10–100 nm thin silicon nitride (SiN_x) window at the center of the nanochannel. When the windows of the two microchips are aligned to overlap, the electron probe may pass through the sample and map the projected charge density in the imaging volume, in this case, that of NP dispersion.

The three common strategies to load pre-synthesized NPs into liquid cell nanochannel are as follows: (1) In “direct loading” the NP solution is pipetted in the liquid cell before the cell is hermetically sealed and inserted into the microscope [9]. Direct loading is a suitable method if the self-assembly reaction is slow and there is sufficient time to start the observation before the system has reached equilibrium in the confined nanochannel. Furthermore, an external biasing method via heating [10], electrochemistry [11], or radiolysis [4] may be used to initiate the self-assembly reaction in the nanochannel. (2) Advanced liquid cell holders equipped with liquid-guiding architecture and pressure-driven

* Corresponding author.

E-mail address: patters3@uci.edu (J.P. Patterson).

<https://doi.org/10.1016/j.ultramic.2023.113865>

Received 21 June 2023; Received in revised form 28 September 2023; Accepted 4 October 2023

Available online 5 October 2023

0304-3991/© 2023 The Author(s). Published by Elsevier B.V. This is an open access article under the CC BY license (<http://creativecommons.org/licenses/by/4.0/>).

pumps [12–14] may flow the NPs into the liquid cell and supply the self-assembly reaction with a sufficient number of colloidal NPs. Even though most of the commercial holders have the flow capability, in the widely used bypass design [15], the flow rate is determined by the relative resistance between the nanochannel and the bypass channel that connects the outlet and inlet ports of the holder. For instance, when a 6 μm spacer thickness was used, a measurable and modeled flow of colloidal spheres through the imaging segment was reported [16]. Elsewhere, the loading of apoferritin-proteins into a nanochannel height of 200 nm failed and physical simulations of the flow pattern confirmed that convection at the center of the liquid cell was likely inefficient due to the geometry of the device [17]. This indicates a challenge for imaging dynamics of low-contrast materials where low liquid thickness is preferred for improved contrast and resolution [5]. Furthermore, small sample volumes may prohibit the use of extended flow times. (3) Finally, the diffusive motion of NPs may be harnessed for NP transport. In this case, the nanochannel needs to be connected to a reservoir of bulk liquid and the net movement of NPs across the concentration gradient takes place spontaneously. The latter approach has the advantage of being suitable for providing mass-transport conditions similar to unstirred bulk liquid. From an imaging point of view, the lack of convection may be beneficial for reducing the motion blur in the recorded data. As a downside, transport by diffusion is effective only at short distances because the loading time (τ) scales with the second power of the net mean displacement ($\langle x \rangle$):

$$\langle x \rangle^2 = 4D\tau \quad (1)$$

where D is the diffusivity of the NP given by the Stokes-Einstein equation [18]:

$$D = \frac{K_b T}{4\pi \eta r} \quad (2)$$

where K_b is the Boltzmann constant, T is the temperature, η is the dynamic viscosity, and r is the radius of the NP. For a 25 nm NP in water, $r=12.5$ nm, $T=293$ K, $K_b=1.38 \times 10^{-23}$ J K⁻¹, $\eta=1 \times 10^{-3}$ Pa, and so $D_{NP}=2.57 \times 10^{-11}$ m² s⁻¹ will be obtained.

Using Eqs. (1) and (2), we obtain $\tau=162$ min for a 25 nm NP traversing a 1 mm 1D nanochannel in ideal conditions where NPs do not interact with the walls of the liquid cell.

However, it is a common observation in LCEM that the free diffusive motion of NPs can be retarded by the walls of the liquid enclosure [9,19,20]. Elsewhere, NPs have been found immobilized at the liquid-solid interface [21,22]. In the latter case, to successfully load the NP dispersion through the nanochannel into the imaging volume, the active surface of the nanochannel needs to be saturated in order to reach the concentration value of the bulk dispersion inside the liquid cell.

To this end, we set to study the effect of attractive wall-NP interaction on the loading time of 25 nm diameter, amino-functionalized silica NPs (SiONP). As a model system, the formation of a randomly packed, colloidal self-assembled monolayer (SAM) on the SiN_x surface was employed. A semi-empirical model for diffusion-propelled mass transport is proposed that can be used to predict the delay when initiating the reaction in the confined imaging volume. The model accounts for the NP D and concentration (c), nanochannel length (l), height (t), and experimentally observed NP surface coverage (φ). Based on the findings, we argue that if the length of the nanochannel distance is made shorter, faster NP loading through the nanochannel can be achieved. Finally, to test this hypothesis, we use a nanofluidic design similar to [12] allowing *in situ* observation of colloidal self-assembly reaction via LCEM.

2. Materials and methods

2.1. Buffer and stock solutions

Phosphate buffered saline (PBS) at pH=2 was prepared by mixing

100 μl of NaH₂PO₄, 120 μl HCl, and 440 μl of NaCl stock solutions, each with a molarity of 1 M and diluting to the final volume of 10 mL. The pH was measured with a digital pH meter (UltraBASIC, Denver Instruments, US). The 1 M stock solutions of NaCl (CELLPURE®, Carl ROTH, Germany) and NaH₂PO₄ were prepared by dissolving each salt in high-performance liquid chromatography (HPLC) -grade water (ROTSOLV®, Carl ROTH, Germany). 1 M stock solution of HCl (AppliChem, Germany) was used as acquired.

2.2. NP dispersion

The SiONPs were synthesized as reported in [23]. Before use, the SiONP dispersion was diluted to a 1:5 vol ratio with PBS pH 2 and shaken resulting in a final silica concentration of 3.22 g l⁻¹. The average ζ -potential of 1:5 diluted SiONP amounted to 13 mV at a pH value of 2 and ionic strength of 0.064 M. The measurement was repeated three times with a Malvern Zetasizer instrument (Malvern Analytical Ltd, UK), and the average value was used. The density (ρ_{SiONP}) of the NPs from a different batch but synthesized in identical conditions was determined by ultracentrifugation and a value of 1630 kg m⁻³ was obtained [24].

2.3. Scanning transmission electron microscopy

Scanning transmission electron microscopy (STEM) was done with a probe-corrected transmission electron microscope (ARM200CF, JEOL, Japan) at acceleration voltage (U) 200 keV and using annular dark-field detector detection mode (DF-STEM). The pixel size (s) and dwell time (τ_{dwell}) were set to 3.1 nm and 5 μs , respectively, corresponding to the nominal magnification of 60 $k\times$. The inner and outer detector DF-collection angles ($\beta_{in}-\beta_{out}$) were set to $\beta_{in}-\beta_{out}=68-280$ mrad. The probe convergence angle amounted to 13.4 mrad for the used 20 μm condenser lens aperture (CLA). The selected spot size of 4C resulted in a probe current (I_p) of 81 pA and an electron dose (D_e) of 2.6 e⁻ Å⁻² per frame.

To collect a sequence of frames with a pre-determined amount and interval, the “STEM Averager”-script for Digital Micrograph software by Dave Mitchell (Release date 15.7.17) was used. Unnecessary electron irradiation of the sample was minimized by setting the beam to automatically park on the silicon frame (outside the window) if the image acquisition was not in progress.

The I_p was measured by directly imaging the probe with the camera (Ultrascan 1000XP, Gatan, Ca, USA) for which the conversion factor (9.9 counts per e⁻) was determined with the built-in picoamperometer of the fluorescent screen. The error of the beam current measurement had been earlier estimated to be ± 10 %. [25] The total D_e was calculated using Eq. (3):

$$D_e = \frac{I_p * \tau_{dwell}}{s^2 * e} \quad (3)$$

where e is the elemental charge.

2.4. Scanning electron microscopy

Scanning electron microscope (Quanta 250 FEG, Thermo Fischer, OR, USA) was operated at 20 keV, and in High Vacuum-mode. Images were captured at magnifications of 76–240 $k\times$, at the working distance of 4–7 mm, $\tau_{dwell}=0.40-1$ μs , and a CLA size of 30 μm resulting in $I_p=0.1$ nA.

2.5. Liquid cell stem

LC-STEM experiments were performed using a liquid flow specimen holder that incorporated tubing for inducing a liquid flow at the tip of the holder (Ocean, DENSSolutions, Netherlands). The lateral size of the

microfluidic chip was 2 mm×2.6 mm and a spacer of 200 nm was used between the chips for defining the t of the nanochannel. The chips were plasma-cleaned for 5 min with a power of 50 W in Ar/O₂-mixture (75 %/25 %) in a chamber that was first evacuated to a vacuum of 70 mTorr (Solaris, GATAN, US). A detailed description for cleaning the specimen holder and microfluidic SiN_x chips has been given in [23].

The nanofluidic design incorporating a microchannel similar to [12] was based on a patent [26] and microchips were custom-made (Norcada, Canada) to meet the following specifications: dimensions of the silicon frame were 2 mm×2.6 mm×0.4 mm and one side was coated with a CVD-grown, 50 nm thick SiN_x film. The window was fabricated via photolithography and wet etching to form an aperture on the vacuum side of the frame so that the final size of the window amounted to 25 μm×400 μm. An additional etching step was performed to fabricate the 0.3 mm wide microchannel on the liquid-facing side of the microchip at a distance of 15 μm from the outer edge of the window. The schematics of the device are given in the Supplementary Information.

The “direct loading” of the SiONP-dispersion was accomplished by pipetting a 1.5 μl droplet of liquid on the bottom microchip and immediately sealing the liquid cell.

To load the sample dispersion “in air”, the flow capability of the sample holder was used. The liquid cell was first assembled in a dry state and inserted in the microscope. After confirming intact windows and a clear field of view (FOV), the tubing of the holder was connected to an external syringe pump loaded with 100 μl of SiONP-dispersion. The liquid flow was sustained for 10 min with the flow speed of 10 μl min⁻¹.

It should be noted that the delay between the plasma cleaning and loading of the SiONP solution may contribute to the affinity [27] between the SiN_x surface, and SiONP, and hence the observed surface coverage. To minimize this effect, all loading experiments were conducted within 30 min after plasma cleaning.

2.6. Measurement of liquid thickness

Electron energy-loss spectroscopy (EELS) was used to determine the presence of the liquid and measure its thickness. Log-ratio method [28] was used in cases where the total relative sample thickness was measured in t/λ , which amounted to less than 5. For details, see [25].

For thicker samples, where the detector counts under the zero-loss peak could not be determined, the liquid thickness was estimated by recording the energy distribution of transmitted electrons and determining the energy at the most probable energy loss as described by the theory by Landau [29]. For a numerical estimate where the contribution of the windows to the total thickness was omitted, Eq. (4) was numerically solved for thickness corresponding to the measured most probable energy loss at the maximum of the plasmon peak.

$$\Delta E_p = \frac{N_A e^4 Z \rho t}{8 \pi \epsilon_0^2 A E_0 \beta^2} \left[\ln \left(\frac{N_A e^4 Z \rho t}{4 \pi \epsilon_0^2 J^2 A (1 - \beta^2)} \right) - \beta^2 + 0.198 \right] \quad (4)$$

where N_A is Avogadro’s number, the root mean squared atomic number of water $Z = \sqrt{\frac{2}{3}Z_H^2 + \frac{1}{3}Z_O^2}$, e is the elemental charge, ϵ_0 is the permittivity of the space, ρ is the density of water, E_0 is the rest mass of an electron, $E_0 = m_0 c^2$, A is the average molar mass of water, $A = \frac{2}{3}M_H + \frac{1}{3}M_O$, and the relativistic factor, $\beta = \frac{v}{c}$, where c is the speed of light and $v = c \sqrt{1 - \frac{1}{\left(\frac{E}{E_0} + 1\right)^2}}$, where electron energy $E = Ue$. J is the mean ionization energy given by $J = 13.5$ Z.

2.7. Image analysis

Image processing software (Fiji distribution of ImageJ-software (v. 1.52i), National Institute of Health, USA) was used for image manipulation, analysis, and drift correction of the recorded data.

The surface coverage of SiONP (φ_{SiONP}) on the SiN_x surface was

determined from the SEM images by segmenting the area covered by SiONP from the bare SiN_x background. In the first step, images were convoluted with the “Gaussian Blur”-function using a kernel diameter of 4 pixels to suppress the noise. Next, pixels representing SiONPs on the sample were segmented by using the “Threshold”-function. The lower limit for the threshold was manually set to a histogram position of local minima, where the populations of background pixels and pixels representing SiONP overlap. The surface area of the SiONP-covered sample surface was obtained by the “Measure”-command. The φ_{SiONP} was calculated by dividing the segmented area by the total area of the image.

The lateral drift present in the experimental data was removed as described in [23].

To improve the SNR in a sequence of images, a custom-made ImageJ script was used to average the indicated number of successive drift-corrected images in a stack.

Background subtraction for the data shown in Fig. 3D was done to remove the artifacts caused by the small, nm-size particles residing on the surface of the window. The background image was created by averaging the first 10 consecutive frames of the dataset total of 90 images. The “Image Calculator”-function in ImageJ was used to subtract the background image from each individual frame.

2.8. Modelling SiONP diffusion in liquid cell

A mathematical equation-solving software (MATLAB, MathWorks, USA) was used to calculate and plot the theoretical values for the τ shown in Fig. 2. of the main text. The Matlab code is provided in the Supplementary Material.

3. Results

3.1. SAM formation on a flat microchip

The impact of confinement on the loading of dispersed SiONPs through a liquid cell’s nanochannel was examined by comparing the SAM formation in bulk and under confinement. Here, two distinct loading strategies were employed to initiate the formation, and after 30 min, the resulting SAMs were visually evaluated for NP coverage on the SiN_x window surface using DF-STEM imaging. In the “direct loading” experiment, a 2 μl drop of SiONP dispersion was pipetted on the bottom microchip after which the liquid cell was sealed with the top microchip and then inserted in the microscope. A SAM had formed on the surface of the window covered with SiONPs. (Fig. 1A). When employing the “in air” loading method, the liquid cell was initially sealed without liquid and inserted in the microscope. A syringe pump connected to the tubing of the holder enabled to flow 100 μl SiONP-dispersion through the tip of the holder with a speed of 10 μl min⁻¹ resulting in a total flow time of 10 min. The microscopy experiment lasted for 90 min, during which only a few SiONPs were spotted in the FOV, but the SAM formation similar to direct loading was not observed (Fig. 1B).

To gain insight into the obstructed SAM formation when under confinement, the sample shown in Fig. 1B was opened and rinsed in a bath of HPLC water and blotted dry with a piece of lint-free tissue. The top microchip was imaged with SEM (Fig. 1C). A clear boundary was observed between the edge and the center of the microchip (dashed line). High-magnification examination with SEM (black boxes) suggested that the highlighted boundary was due to the formation of SAM that took place only in the vicinity of the microchip edge (Fig. 1D). Image analysis indicated φ_{SiONP} of 0.7. Lower coverage of SiONP was found when images were acquired at the center of the cell (Fig. 1E). The observation suggested hindered mass transport in the liquid cell leading to uneven distribution of SiONPs along the nanochannel.

3.2. Modelling NP diffusion in a nanochannel

To predict and control colloidal assembly in the nanochannel it is

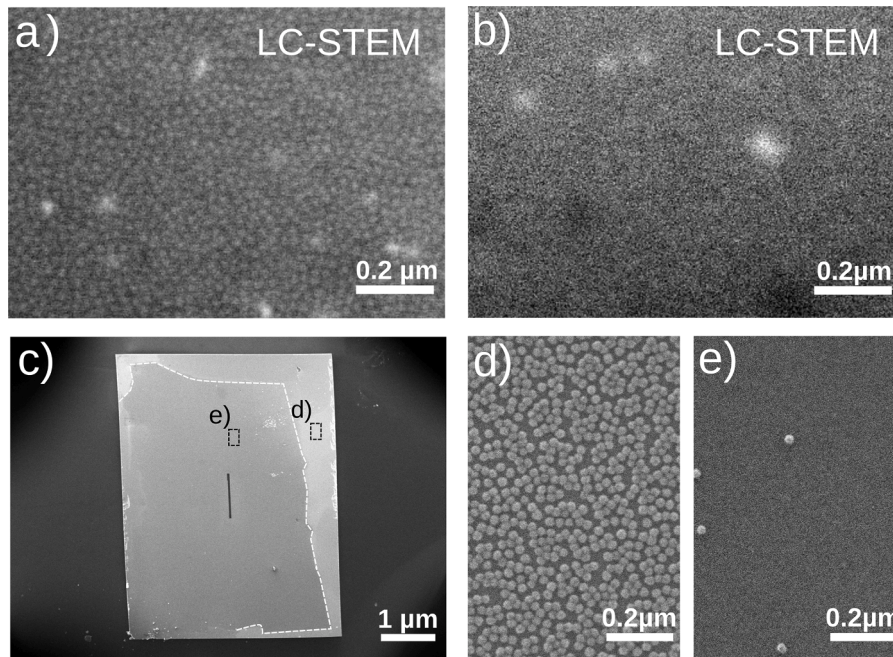


Fig. 1. Two sample loading strategies were compared after 30 min to assess their efficiency in forming a colloidal self-assembled monolayer (SAM) in a liquid-cell scanning transmission electron microscopy (LC-STEM) experiment. Panel A) shows the resulting SAM when the “direct loading”-method was used to load functionalized silica NP (SiONP) dispersion in the liquid cell. 30 consecutive frames were averaged resulting in an electron dose (D_e) of $79 \text{ e}^- \text{ \AA}^{-2}$. In B) the resulting SAM is shown for the liquid cell assembled “in air” where the SiONP-dispersion was loaded *in situ* by using flow. Here, 20 consecutive frames were averaged resulting in $D_e=53 \text{ e}^- \text{ \AA}^{-2}$. In A) and B), the relative sample thicknesses (t/λ) amounted to 4.5 and 4.0, which corresponded to liquid thicknesses (t) of 660 nm and 570 nm, respectively. (C) The liquid cell from B) was examined with scanning electron microscopy (SEM) after the LC-STEM experiment. In (D) the SAM had formed on the area close to the edge of the microchip. E) Only a few particles were found when examining the center of the liquid cell. For (C–E), water was first flowed through the cell after which the microchips were rinsed in a bath of water and blotted dry before imaging in SEM.

essential to understand the time scale of diffusive transport that moves NPs toward the imaging volume. The mass transport via steady-state diffusion is described by Fick’s first law stating the flux (J) of particles depends on the D and the fixed concentration gradient in the system: [30]

$$J = -D \frac{\partial c}{\partial x} \quad (5)$$

The presence of liquid enclosure walls was omitted in the first stage of calculations. A solution (Eq. (6)) to the diffusion equation was adapted from [30] and was used to model how steady-state diffusion drove the concentration gradient over time (τ) in a system where a point source of contamination, here SiONP, at a constant concentration (c_o), was located at a distance (l) from the point of reference, that is, the imaging volume of the liquid cell.

$$c(l, \tau)_{channel} = c_o \left(1 - \text{erf} \left(\frac{l}{\sqrt{4D\tau}} \right) \right) \quad (6)$$

It is reasonable to assume a constant bulk concentration as the volume of the confined liquid for a $0.2 \mu\text{m}$ spacer is in the order of $1\text{--}2 \text{ nl}$, while the volume of the bulk liquid is approximately $50 \mu\text{l}$ (including the tubing used to connect the syringe pump and the holder assembly).

An approximation was made, where the cross-sectional concentration profile was assumed to be uniform in all the calculations. The analysis was constrained to a nanochannel of the width (w) $1 \mu\text{m}$ and height (h) $0.5 \mu\text{m}$ by projecting the unit volume concentration (NPs m^{-3}) to unit length concentration (NPs m^{-1}) by multiplying the original concentration by w and h of the channel.

$$c_o = c * w * l \quad (7)$$

where c was obtained by calculating the number of SiONP in the unit volume based on the known mass concentration of the silica precursor

(c_{Si}) and density (ρ_{SiONP}) and volume (V_{SiONP}) of the SiONP with radius (r) of 12.5 nm

$$c = \frac{c_{Si}}{V_{SiONP} \rho_{SiONP}} = \frac{c_{Si}}{\frac{4}{3} \pi r^3 \rho_{SiONP}} \quad (8)$$

Thus, the used concentration describes the number of particles that reside in the channel per unit length instead of the typical unit volume. In Fig. 2A, Eq. (6) has been plotted for $\tau=10, 100, 1000,$ and $10,000 \text{ s}$.

Next, the required number of NPs that needed to reach the window with dimensions ($L=w=1 \mu\text{m}$) to result in the experimentally found $\varphi_{SiONP}=0.7$ was calculated via

$$N_{window} = \frac{A_{window}}{A_{SiONP}} * \varphi_{SiONP} = \frac{w * L}{2\pi r^2} * 0.7 \quad (9)$$

To calculate the number of SiONPs that have reached the window of size $1 \mu\text{m}$ by $1 \mu\text{m}$, located at $l=x$ for a given τ , numerical integration was performed in equation-solving software (Matlab).

$$N_{tail} = \int_{l=x}^{\infty} c(l, \tau)_{channel} dl \quad (10)$$

Now, it was assumed that all the particles immobilized on the surface of the window as soon as they passed its edge. The Matlab script was looped for τ (step time 10 s) until $N_{tail}=N_{window}$ and resulted in $\tau=140 \text{ min}$ for full coverage of SiONP on the window. This is in reasonable agreement with the value $\tau=162 \text{ min}$ obtained for the mean displacement over a distance of 1 mm (Eq. (1)).

In the next step, the model was expanded to account for the SiONPs’ tendency to adhere to the exposed SiN_x surface as they pass through the nanochannel. The additional number of SiONP needed to saturate the walls was calculated based on the surface area of the channel ($A_{channel}$), the area of the NP (A_{SiONP}), and the experimentally observed φ_{SiONP} (Fig. 1D).

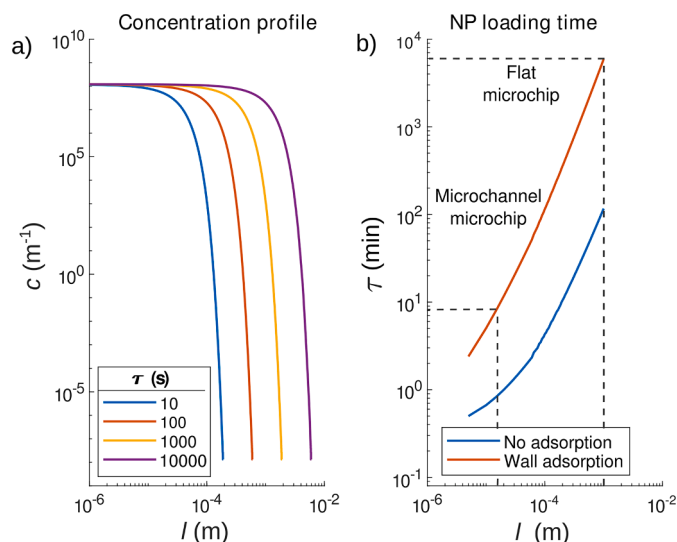


Fig. 2. Modeling the concentration gradient (c) and resulting loading time (τ) for SiONP during an *in situ* LCEM experiment. To illustrate the gradual spreading of SiONP in the nanochannel of length (l), Eq. (6) was plotted in (A) for a range of diffusion time values. In (B) the τ was numerically solved for obtaining SiONP coverage (φ_{SiONP}) of 0.7 in a 500 nm thin nanochannel. In the first case, all the wall effects were excluded (No adsorption). In the second case, it was assumed that SiONPs saturate the walls of the liquid cell before reaching the imaging volume (Wall adsorption). Locations of the window in flat and microchannel microchip-based nanofluidic designs are indicated at $l=1$ mm and $l=15$ μ m, respectively. The Matlab code is available in the Supplementary Material.

$$N(l)_{\text{channel}} = 2 * \frac{A_{\text{channel}}}{A_{\text{SiONP}}} * \varphi_{\text{SiONP}} = 2 * \frac{l * w}{A_{\text{SiONP}}} * 0.7 \quad (11)$$

To account for the additional time required to saturate the nanochannel walls, it was assumed that the average flux of SiONP was equal with and without wall adsorption for a given l . The rationale of this assumption is that according to Fick's law, the net J is time-independent and depends only on D and the concentration gradient present in the system (Eq. (5)).

The number of SiONPs ($N(\tau_n)$) residing in the whole channel at a certain time point (τ_n) was calculated by numerical integration

$$N(\tau_n) = \int_{l=0}^{\infty} c(l, \tau_n)_{\text{channel}} dl \quad (12)$$

The flux (NP m⁻¹ s⁻¹) for a given channel length at τ_n was obtained by

$$J = \frac{N(\tau_n) - N(\tau_{n-1})}{\tau_n - \tau_{n-1}} \quad (13)$$

The average flux (J_{avg}) for a given channel length was obtained by averaging J over all the time points.

Finally, the additional time required to fill the nanochannel walls was obtained by

$$t = \frac{N(l)_{\text{channel}}}{J_{\text{avg}}(l)} \quad (14)$$

For $l=1$ mm, a total time of 7084 min (4.9 days) was obtained until full coverage could be expected at the location of the window on the microchip (Fig. 2B). Such a timespan for a single experiment renders the approach unpractical for at least two foreseeable reasons: First, blocking an electron microscope for several days is not an ideal use of resources and secondly, extended exposure of the liquid sample may lead to unwanted beam-induced effects.

3.3. Microchannel microchip

To facilitate the loading of SiONPs to the imaging volume, a nanofluidic design similar to [12] was tested where a patented [26] microchannel concept effectively reduced the required l from 1000 μ m down to 15 μ m (Schematics given in Supplementary Information). The length of the nanochannel was dictated by the accuracy and precision of the fabrication process. We estimated that the relative location of the window and the microchannel edges can be reliably fabricated on a wafer scale at an accuracy of 5 μ m. To minimize the risk of fabricating faulty devices where the etching patterns of the window and microchannel overlap, likely leading to compromised mechanical stability of the SiN_x membrane, we chose the distance to be 15 μ m.

Based on the diffusion-propelled loading model presented above, we anticipated a loading time of $\tau=50$ s for free Brownian motion, and $\tau=9$ min if adsorption on the wall was enabled (Fig. 2B). We also performed a sensitivity analysis on how the experimental variables, c , and t , affected the outcome of the calculated loading time when the wall adsorption was enabled. (See Supplementary Information). Interestingly, it was found that if the t was reduced from 0.5 to 0.1 μ m, the expected diffusion time increased from 8 to 130 min, while increasing t to 1 μ m resulted in a loading time of 3 min.

To evaluate the performance of microchannel liquid cell in imaging colloidal dynamics with LCEM, an experiment was conducted to test if the experimental loading time of SiONP had improved in the imaging volume. A microchannel microchip was placed on the bottom of the holder tip, and a regular microchip with a 0.2 μ m spacer was placed on top. The cell was sealed, and the holder was inserted into the microscope and connected to a syringe pump loaded with SiONP dispersion (Fig. 3A-C). The experiment was initiated by starting the syringe pump and image acquisition simultaneously so that a single frame was recorded every 20.16 s. By using the flow speed of 20 μ l min⁻¹, a total of 60 μ l of SiONP in PBS pH 2 was flowed through the system. The liquid appeared on the window 90 s after starting the flow and was sustained for another 90 s before the syringe pump was turned off. After approximately 15 min the liquid had appeared in the FOV, some aggregates were seen to move across the FOV, and the focus was slightly corrected to counteract the stage drift in the z-direction. The data acquisition was resumed until 100 frames were acquired. Three snapshots from the experiment are shown in Fig. 3D where 30 frames have been averaged to improve the poor SNR in the images showing the appearance of SiONP in the FOV during the experiment (see the video in the Supplementary Material). The liquid thickness was too thick for determination using the EELS log-ratio method, and the most probable energy loss of the plasmon peak [29] was found to be at 205 eV corresponding to a liquid thickness of 1 μ m.

LCEM experiment was followed by a posterior analysis with SEM. The shape of the microchannel can be seen on the opposite spacer microchip (Fig. 3E) and was caused by the SiONPs that had adhered to the SiN_x surface (Fig. 3F). SEM imaging of the area where the dataset shown in panel A was acquired revealed a rectangular-shaped region that had a lower coverage of SiONP compared to the surrounding area (Fig. 3G). The rectangular shape is the result of the scanning pattern of the STEM probe.

4. Discussion

To summarize, industry-standard flat microchips together with "in air" loading method were used to initiate a colloidal assembly reaction during a LCEM experiment *in situ*. Results indicated that the dispersed SiONPs adhered on the edges of the formed nanochannel but did not reach the imaging volume at the center of the liquid cell, albeit the liquid medium appeared in the FOV once the flow had been enabled. As a result, we were not able to observe the SAM formation *in situ* and suspected that the reason for this was the poor mass-transport of SiONPs in the nanochannel: first, the high aspect ratio (h/l) of the liquid cell led to poor flow characteristics, as has been reported in [17]. Secondly, the

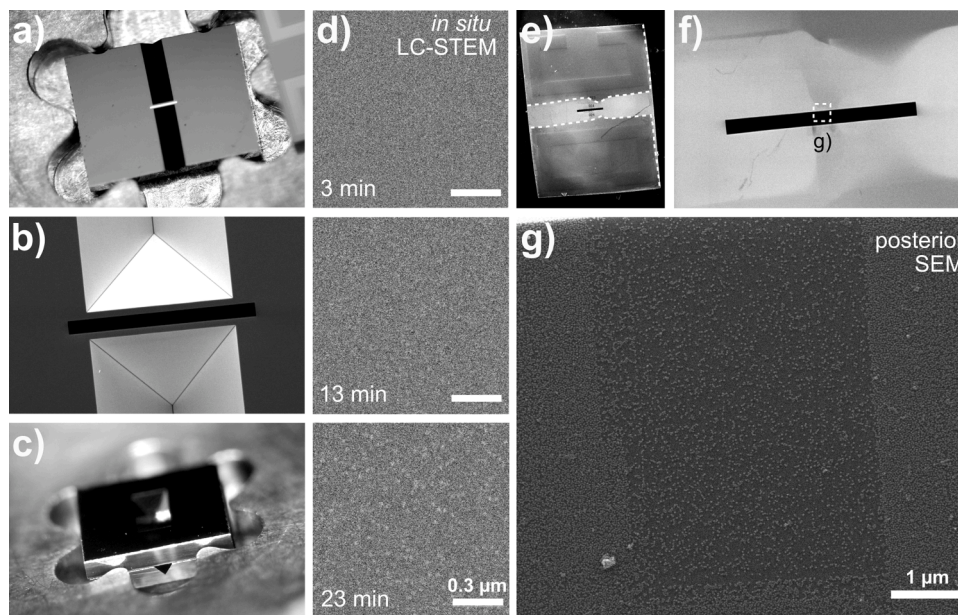


Fig. 3. Directly observing the formation of SAM in a nanofluidic device with microchannel geometry architecture similar to [12,26]. (A) Photograph of the liquid-guiding microchannel microchip, with the microchannel aligned vertically and the 400 μm long and 25 μm wide window positioned in the middle. (B) Shows a magnification of the liquid cell window. The distance between the edge of the window and the microchannel amounted to $l=15 \mu\text{m}$. (C) A photograph of the assembled nanofluidic device where a microchannel microchip is stacked under a flat microchip with 0.2 μm thick spacer. In (D), three frames from an LC-STEM *in situ* experiment are shown as recorded at different time points indicating the appearance of SiONPs at approximately 18 min on the windows after the liquid had appeared in the FOV (Supplementary Material video). Images were acquired in DF-STEM mode using the same settings as in Fig. 1A, B), and here 30 frames were averaged in the post-processing step resulting in $D_e=79 \text{ e}^- \text{ \AA}^{-2}$. The EELS measurement indicated the plasmon peak at 205 eV, corresponding to a sample thickness of 1 μm . (E) A posterior SEM image of the flat spacer microchip was acquired after opening and rinsing the liquid cell. Contrast variation is present along the area opposing the microchannel (dashed line) and faint bumps on the flat surface are due to the spacer layer. (F) A magnification of the nanochannel location. In (G) a further magnification of the window area shows the region irradiated during the *in situ* experiment shown in panel (D).

attractive interaction between the amino-functionalized SiONPs and O_2 plasma-treated membrane may have further slowed down the effective speed at which the SiONPs traversed through the nanochannel formed between the microchips. To provide a quantitative explanation for the results, a semi-empirical model based on the 1D diffusive motion was developed where the experimental parameters were SiONP diffusivity and concentration, nanochannel length, height, and experimentally observed surface coverage. For an industry-standard flat microchip ($l=1 \text{ mm}$) the model predicted a loading time of nearly five days and supported the idea that a shorter nanochannel could greatly facilitate the loading of SiONP *in situ*.

The prediction derived from the modeling was assessed by using a custom-made liquid cell in which a microchannel [12,26] had been etched on one of the microchips, effectively reducing the nanochannel length to $l=15 \mu\text{m}$. The microchannel liquid cell did enable observation of the SAM formation at 18 min after the liquid had appeared in the FOV. This was an improvement in comparison to the flat microchip and agreed with the proposed 1D diffusion model that predicted a retention time of 9 min. A possible reason that our diffusion model was found to be off by a factor of two is that it did not account for the effect of confinement on the diffusivity of SiONP. It has been reported that in nanochannels with heights less than 1 μm , a reduction of 30–70 % has been found in the diffusivity [31–33] and could explain the longer retention time in the nanochannel. Another likely reason for the disagreement was the experimental uncertainty related to t . The sensitivity analysis indicated that when t was in the range of 0.1–1 μm , resulting loading times could vary between 131 and 3 min, respectively, that is, nearly two orders of magnitude. Yet, to avoid unnecessary electron irradiation during an LCEM experiment, the characteristic time scale needs to be defined so that the imaging can be started precisely as the NPs appear at the window. In practice, this can be challenging unless experimental parameters such as t can be controlled with high precision.

Here, monolithic liquid cell architecture [34] may provide more precise nanochannel height and result in improved reproducibility in the experimental work.

The posterior SEM analysis indicated that the electron beam locally reduced the coverage of the SiONPs, Fig. 3G. We hypothesize that the electron beam changed the surface properties of the window, thus resulting in the formation of a lower-density SAM. It is well established that electron beam effects can control colloidal assembly and interactions during LCEM experiments [4]. A possible explanation for the reduced surface coverage observed here is the surface chemistry of the SiN_x . The solvated electrons could have reduced silanol groups, which led to the weaker negative surface charge of the SiN_x -membrane and hence reduced attractive electrostatic force with SiONPs carrying a positive charge.

5. Conclusions

We have proposed a semi-empirical model for diffusive mass transport, that can be used to explain the delays related to the loading of NPs to the imaging volume of a liquid cell. The model accounts for the NP diffusivity and concentration, nanochannel length, height, and experimentally observed surface coverage. Based on the findings, a common liquid-guiding nanofluidic design was tested where a factor of 70 shorter nanochannel facilitated diffusive mass transport in the liquid cell and allowed observation of colloidal self-assembly reaction *in situ*. The combination of the diffusion model with such microchannel architecture may open up new ways to control self-assembly reactions during a LCEM experiment and to study electron beam-induced effects in colloidal systems. In future work, the use of a more rigorous modeling tool for the diffusive mass transport, for example, employing 2D finite element analysis, could offer a more detailed view of the NP dynamics in the nanochannel. Furthermore, using suitable monolithic liquid cell

architecture with precise nanochannel height would enable a more accurate comparison of results from computational and experimental methods.

Funding sources

We acknowledge funding by the Marie Skłodowska-Curie ITN project MULTIMAT. P.K. acknowledges funding from the European Union's Horizon 2020 research and innovation program under Grant Agreement No. 101017902.

Supplementary material

The following files are available free of charge: Supplementary Information file (.pdf) – Schematics of the microchannel microchip and sensitivity analysis for the modeled loading time.

Supplementary video (.mp4) – Data from a LCEM experiment where SiONPs were loaded in the field of view (Fig. 3D). In the video, the time stamp indicates the time after the liquid had appeared in the field of view.

Supplementary code (.txt) – The Matlab code includes all the numerical calculations discussed in the main text and Fig. 2

CRediT authorship contribution statement

Peter Kunnas: Investigation, Supervision, Methodology, Writing – original draft. **Niels de Jonge:** Investigation, Writing – original draft. **Joseph P. Patterson:** Investigation, Writing – review & editing.

Declaration of Competing Interest

The authors declare the following financial interests/personal relationships which may be considered as potential competing interests: Niels de Jonge has patent #US20120120226A1 issued to Niels de Jonge.

Data availability

Data will be made available on request.

Acknowledgments

The authors like to thank Sebastian Rzakiewicz for synthesizing the SiONPs and for discussions. Dr. Xufen Xu and Dr. Deniz Eren are acknowledged for discussions about the density and zeta potential of colloidal particles used in this work, Dr. Isabella Tavernano for measuring the zeta potential of SiONP dispersion, and M.Sc. Florian Sauer for the discussions about modeling the concentration gradient in a liquid cell. We want to thank Norcada for the fabrication of the new microchannel microchips. We thank Eduard Arzt for his support through INM, Saarbrücken.

During the preparation of this work, the author(s) used “Wordtune” service in order to facilitate proofreading and to improve the readability of the manuscript. After using this tool/service, the author(s) reviewed and edited the content as needed and take(s) full responsibility for the content of the publication.

Supplementary materials

Supplementary material associated with this article can be found, in the online version, at [doi:10.1016/j.ultramic.2023.113865](https://doi.org/10.1016/j.ultramic.2023.113865).

References

- [1] J. van der Gucht, Grand challenges in soft matter physics, *Front. Phys.* 6 (2018) 87, <https://doi.org/10.3389/FPHY.2018.00087>.

- [2] C.A.S. Batista, R.G. Larson, N.A. Kotov, C.A. Silvera Batista, R.G. Larson, N. A. Kotov, Nonadditivity of nanoparticle interactions, *Science* 350 (2015), 1242477, <https://doi.org/10.1126/science.1242477>.
- [3] D.J. Kelly, M. Zhou, N. Clark, M.J. Hamer, E.A. Lewis, A.M. Rakowski, S.J. Haigh, R.V. Gorbachev, Nanometer resolution elemental mapping in graphene-based TEM liquid cells, *Nano Lett.* 18 (2018) 1168–1174, <https://doi.org/10.1021/acs.nanolett.7b04713>.
- [4] Z. Ou, Z. Wang, B. Luo, E. Luijten, Q. Chen, Kinetic pathways of crystallization at the nanoscale, *Nat. Mater.* 19 (2020) 450–455, <https://doi.org/10.1038/s41563-019-0514-1>.
- [5] N. de Jonge, Theory of the spatial resolution of (scanning) transmission electron microscopy in liquid water or ice layers, *Ultramicroscopy* 187 (2018) 113–125, <https://doi.org/10.1016/j.ultramic.2018.01.007>.
- [6] B. Li, D. Zhou, Y. Han, Assembly and phase transitions of colloidal crystals, *Nat. Rev. Mater.* 1 (2016) 15011, <https://doi.org/10.1038/natrevmats.2015.11>.
- [7] V. Lotito, T. Zambelli, Approaches to self-assembly of colloidal monolayers: a guide for nanotechnologists, *Adv. Colloid Interface Sci.* 246 (2017) 217–274, <https://doi.org/10.1016/J.CIS.2017.04.003>.
- [8] J.R. Dwyer, Y.M.N.D.Y. Bandara, J.C. Whelan, B.I. Karawdeniya, J.W. Nichols, Chapter 7. Silicon Nitride Thin Films for Nanofluidic Device Fabrication, in: J. Edel, A. Ivanov (Eds.), *Nanofluidics*, 2016, pp. 190–236, <https://doi.org/10.1039/9781849735230-00190>.
- [9] A. Verch, M. Pfaff, N. De Jonge, Exceptionally slow movement of gold nanoparticles at a solid/liquid interface investigated by scanning transmission electron microscopy, *Langmuir* 31 (2015) 6956–6964, <https://doi.org/10.1021/acs.langmuir.5b00150>.
- [10] K.J. Isaacson, B.R. Van Deventer, D.B. Steinhilber, M.M. Jensen, J. Cappello, H. Ghandehari, Liquid-cell transmission electron microscopy for imaging of thermosensitive recombinant polymers, *JCR* 344 (2022) 39–49, <https://doi.org/10.1016/J.JCONREL.2022.02.019>.
- [11] T. Yamazaki, H. Niinomi, Y. Kimura, Feasibility of control of particle assembly by dielectrophoresis in liquid-cell transmission electron microscopy, *Microscopy* 71 (2022) 231–237, <https://doi.org/10.1093/jmicro/dfac021>.
- [12] C. Mueller, M. Harb, J.R. Dwyer, R.J.D. Miller, Nanofluidic cells with controlled pathlength and liquid flow for rapid, high-resolution *in situ* imaging with electrons, *J. Phys. Chem. Lett.* 4 (2013) 2339–2347, <https://doi.org/10.1021/jz401067k>.
- [13] A.F. Beker, H. Sun, M. Lemang, J.T. Van Omme, R.G. Spruit, M. Bremmer, S. Basak, H.H. Pérez Garza, *In situ* electrochemistry inside a TEM with controlled mass transport, *Nanoscale* 12 (2020) 22192–22201, <https://doi.org/10.1039/d0nr04961a>.
- [14] S. Merckens, G. De Salvo, J. Kruse, E. Modin, C. Tollan, M. Grzelczak, A. Chuvilin, Quantification of reagent mixing in liquid flow cells for liquid phase-TEM, *Ultramicroscopy* (2022), 113654, <https://doi.org/10.1016/j.ultramic.2022.113654>.
- [15] H. Wu, H. Friedrich, J.P. Patterson, N.A.J.M. Sommerdijk, N. Jonge, Liquid-phase electron microscopy for soft matter science and biology, *Adv. Mater.* 32 (2020), 2001582, <https://doi.org/10.1002/adma.202001582>.
- [16] E.A. Ring, N. De Jonge, Microfluidic system for transmission electron microscopy, *Microsc. Microanal.* 16 (2010) 622–629, <https://doi.org/10.1017/s1431927610093669>.
- [17] G. Marchello, C. De Pace, N. Wilkinson, L. Ruiz-Perez, G. Battaglia, 4D liquid-phase electron microscopy of ferritin by brownian single particle analysis, preprint in arxiv. org. (2019). <http://arxiv.org/abs/1907.03348>.
- [18] A. Einstein, Über die von der molekularkinetischen Theorie der Wärme geforderte Bewegung von in ruhenden Flüssigkeiten suspendierten Teilchen, *Ann. Phys.* 322 (1905) 549–560, <https://doi.org/10.1002/ANDP.19053220806>.
- [19] L.R. Parent, E. Bakalis, M. Proetto, Y. Li, C. Park, F. Zerbetto, N.C. Gianneschi, Tackling the challenges of dynamic experiments using liquid-cell transmission electron microscopy, *Acc. Chem. Res.* 51 (2018) 3–11, <https://doi.org/10.1021/acs.accounts.7b00331>.
- [20] T.J. Woehl, T. Prozorov, The mechanisms for nanoparticle surface diffusion and chain self-assembly determined from real-time nanoscale kinetics in liquid, *J. Phys. Chem. C* 119 (2015) 21261–21269, <https://doi.org/10.1021/acs.jpcc.5b07164>.
- [21] I.M. Abrams, J.W. McBain, A closed cell for electron microscopy, *Science* 100 (1944) 273–274, <https://doi.org/10.1126/science.100.2595.273>.
- [22] A.W. Robertson, G. Zhu, B.L. Mehdi, R.M.J. Jacobs, J. De Yoreo, N.D. Browning, Nanoparticle immobilization for controllable experiments in liquid-cell transmission electron microscopy, *ACS Appl. Mater. Interfaces* 10 (2018) 22801–22808, <https://doi.org/10.1021/acsami.8b03688>.
- [23] P. Kunnas, M.A. Moradi, N. Sommerdijk, N. de Jonge, Strategy for optimizing experimental settings for studying low atomic number colloidal assemblies using liquid phase scanning transmission electron microscopy, *Ultramicroscopy* 240 (2022), 113596, <https://doi.org/10.1016/J.ULTRAMIC.2022.113596>.
- [24] X. Xu, T. Franke, K. Schilling, N.A.J.M. Sommerdijk, H. Cölfen, Binary colloidal nanoparticle concentration gradients in a centrifugal field at high concentration, *Nano Lett.* (2019) 1–10, <https://doi.org/10.1021/acs.nanolett.8b04496>.
- [25] S. Keskin, P. Kunnas, N. De Jonge, Liquid-phase electron microscopy with controllable liquid thickness, *Nano Lett.* 19 (2019) 4608–4613, <https://doi.org/10.1021/acs.nanolett.9b01576>.
- [26] de Jonge, N.; Transmission electron microscopy for imaging live cells, US Patent US20120120226A1, May 17, 2012. <https://patents.google.com/patent/US9207196B2>.
- [27] J.P. Patterson, P. Abellan, M.S. Denny, C. Park, N.D. Browning, S.M. Cohen, J. E. Evans, N.C. Gianneschi, Observing the growth of metal-organic frameworks by *in situ* liquid cell transmission electron microscopy, *J. Am. Chem. Soc.* 137 (2015) 7322–7328, <https://doi.org/10.1021/jacs.5b00817>.

- [28] T. Malis, S.C. Cheng, R.F. Egerton, EELS log-ratio technique for specimen-thickness measurement in the TEM, *J. Electron Microsc. Tech.* 8 (1988) 193–200, <https://doi.org/10.1002/jemt.1060080206>.
- [29] H. Kohl, L. Reimer, *Transmission Electron Microscopy*, 5th ed., Springer New York, New York, NY, 2008 <https://doi.org/10.1007/978-0-387-34758-5>.
- [30] B.S. Bokstein, M.I. Mendeleev, D.J. Srolovitz, *Thermodynamics and Kinetics in Materials Science*, Oxford University Press, 2005, <https://doi.org/10.1093/oso/9780198528036.001.0001>.
- [31] N. Kaji, R. Ogawa, A. Oki, Y. Horiike, M. Tokeshi, Y. Baba, Study of water properties in nanospace, *Anal. Bioanal. Chem.* 386 (2006) 759–764, <https://doi.org/10.1007/s00216-006-0469-3>.
- [32] H.T. Hoang, I.M. Segers-Nolten, N.R. Tas, J.W. van Honschoten, V. Subramaniam, M.C. Elwenspoek, Analysis of single quantum-dot mobility inside 1D nanochannel devices, *Nanotechnology* 22 (2011), 275201, <https://doi.org/10.1088/0957-4484/22/27/275201>.
- [33] K. Pappaert, J. Biesemans, D. Clicq, S. Vankrunkelsven, G. Desmet, Measurements of diffusion coefficients in 1-D micro- and nanochannels using shear-driven flows, *Lab Chip* 5 (2005) 1104–1110, <https://doi.org/10.1039/B505122C>.
- [34] M.N. Yesibolati, S. Laganà, H. Sun, M. Beleggia, S.M. Kathmann, T. Kasama, K. Mølhave, Mean inner potential of liquid water, *Phys. Rev. Lett.* 124 (2020), 065502, <https://doi.org/10.1103/physrevlett.124.065502>.